Laboratory Modelling of Sill Emplacement: Part 1 – saucer-shaped intrusions

Uchitha N. Arachchige[1], Alexander R. Cruden[1], Roberto Weinberg[1], Anja Slim[1], Jonas Köpping[1]

[1]School of Earth, Atmosphere and Environment, Monash University, 9 Rainforest Walk, Clayton, VIC 3800, Australia

Abstract

We investigate the conditions under which saucer-shaped sills form through the upper crust and their geometries. We performed a series of scaled laboratory experiments that employ visco-elastic-plastic Laponite RD® (LRD) gels to model upper crustal rocks, and Newtonian paraffin oil as the magma analogue. Both homogenous and layered analogue upper crust is considered. In homogenous 3 wt. % LRD, the injected oil formed a saucer-shaped intrusion with the shortest inner sill observed among all of the experiments. Saucer-shaped sills always formed in experiments with a two-layer upper crust. These experiments show sharp transitions from an inner flat sill to outer inclined sheets, which are characterised by non-planar margins. The experimental results show that: (1) the transition from an inner flat sill to outer inclined sheet occurs when the sill radius to overburden depth ratio (r/H) is between 0.5 and 2.5; (2) the inclined sheets propagate upwards with angles, $\theta = 15°$ to 25°; (3) the ratio of the Young's modulus (E*) between the layers controls when the inner flat sill to outer inclined sheet occurs; and (4) irregular finger-like and/or lobe segment geometries form at the propagating tip of the intrusion. The results also suggest that there is no strict requirement for high horizontal stresses to form natural saucer-shaped sill geometries. We conclude that the layered visco-elastic-plastic crustal analogues better represent natural, complex saucer-shaped sill geometries. Furthermore, the observed sharp transitions between inner and outer sills are compatible with brittle-elastic fracture mechanisms operating at the intrusion scale.

Plain language summary

When magma rise through the Earth's crust to the surface, it forms cracks within rock layers, which propagate upwards with the magma inside. These cracks often form "saucer-shaped sill" structures which transport magma horizontally and vertically within its inner flat and outer inclined regions, respectively. In order to understand how these saucer-shaped sills form and propagate within rock layers, we model them with experimental methods using similar

conditions to the nature and analyse the results of the experiments. In our experiments, Laponite RD® and paraffin oil represent the host rock and the ascending magma, respectively. We find that the saucer-shaped sills consist of sharp transitions from inner flat to outer inclined regions. Moreover, the leading edges of these cracks are irregular, which consists of finger and lobe shaped margins. Results suggest that the material properties of Laponite RD® better represent the natural rock behaviour and produce much similar saucer-shaped sills that of in nature. However, the experimental sills are more complex than previously modelled and future planning efforts should take these results into account.

1. Introduction

Igneous sheet intrusions such as dykes and sills are broadly planar structures that are the principal pathways for the migration of magma through the upper crust. Although dykes have traditionally been considered to play the dominant role in magma plumbing systems, recent three dimensional (3D) seismic reflection studies of offshore sedimentary basins suggest that mafic sill complexes play a major, and perhaps leading, role in the vertical and horizontal transport of magma in the shallow crust (Magee et al., 2016; Eide et al., 2017). Such sill complexes often comprise non-planar, interconnected saucer-shaped sills and inclined, strata-discordant intrusions (Thomson and Hutton, 2004; Hansen and Cartwright, 2006).

Saucer-shaped sill morphologies are regarded to be a fundamental feature of mafic intrusions in shallow sedimentary basins (Galland et al., 2009; Galland & Scheibert, 2013; Chen et al., 2017). Field observations (e.g., Golden Valley Sill Complex, South Africa; Chevallier and Woodford, 1999; Planke et al., 2005; Planke, 2008) and two-dimensional (2D) and 3D seismic reflection observations (Hansen et al., 2004; Thomson and Hutton, 2004; Hansen and Cartwright, 2006; Hansen et al., 2008) of saucer-shaped sills indicate that they comprise a sub-horizontal, strata-concordant, inner sill, forming the base, and an inclined, strata-discordant, concave upward outer section (Figs. 1a, 2a). Field observations and 3D seismic surveys have also found that these intrusions can have non-planar, segmented outer margins consisting of lobes and fingers that range in scale from metres to kilometres (Pollard et al., 1975; Thomson and Hutton, 2004; Hansen and Cartwright, 2006; Magee et al., 2016).

The emplacement mechanisms of saucer-shaped sills are mainly attributed to either the elastic or plastic properties of the host rocks, as well as interaction with Earth's free surface. By considering the Mode I and Mode II stress intensity factors at the tip of a horizontal fluid-filled fracture in an elastic medium with a free upper surface, Pollard and Holzhausen (1978) showed that horizontal sills transition into inclined sheets when their depth is less than two-

times their radius. This finding is supported by numerical (e.g. Malthe-Sørenssen. et al., 2004; Walker and Gill, 2020) and analogue models (e.g. Bunger et al., 2008) using elastic host rocks, which found that saucer-shaped sills form due to the mechanical interplay between elastic deformation around the growing sill and upward displacement of the overburden towards a free upper surface (Figs. 1b, d). However, models of Walker and Gill (2020) and Bunger et al. (2008) require quite high horizontal stresses to produce geometries that approach those observed in nature (Fig. 2c).

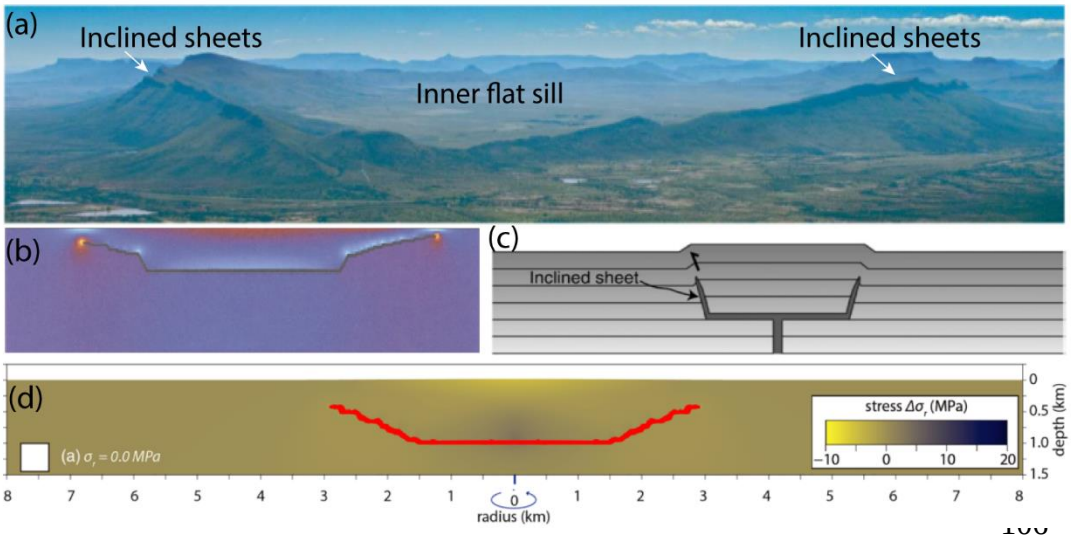

Figure 1. *(a) Oblique aerial view of the Golden Valley sill in the Karoo basin, South Africa showing an inner flat sill and outer inclined sheets (from Polteau et al. 2008). (b) Numerical simulation by Malthe-Sørenssen et al. (2004) showing upward deflection due to the elastic interaction with the overburden. (c) Schematic showing the overburden uplift and corresponding shear fault development due to sill inflation, resulting in inclined sheets (from Galland et al. 2009). (d) Numerical simulation by Gill and Walker (2020) showing the morphology of a saucer-shaped sill in the absence of a horizontal tectonic compressional stress.*

A recent numerical analysis by Haug et al. (2017) using rigid-plasticity theory in a homogenous Mohr-Coulomb material showed that saucer-shaped sills can also be created due to inelastic damage (i.e., shear failure) caused by an inflating flat sill (Fig. 2c). Furthermore, analogue experiments using granular Mohr-Coulomb host-rock materials that undergo plastic deformation also formed saucer-shaped sills (Mathieu et al., 2008; Galland et al., 2009) (Fig.

1c). However, inner sill to inclined sheet transitions, sill inclinations and overall geometries of saucer-shaped sills of these numerical (Fig. 1b) and experimental models (Fig. 1c) do not match with those in nature (Fig. 1a). Furthermore, experiments using brittle-elastic gelatine, a common host rock analogue, have successfully produced sills and dykes but not saucer-shaped sills (Kavanagh et al., 2006, 2015, 2018).

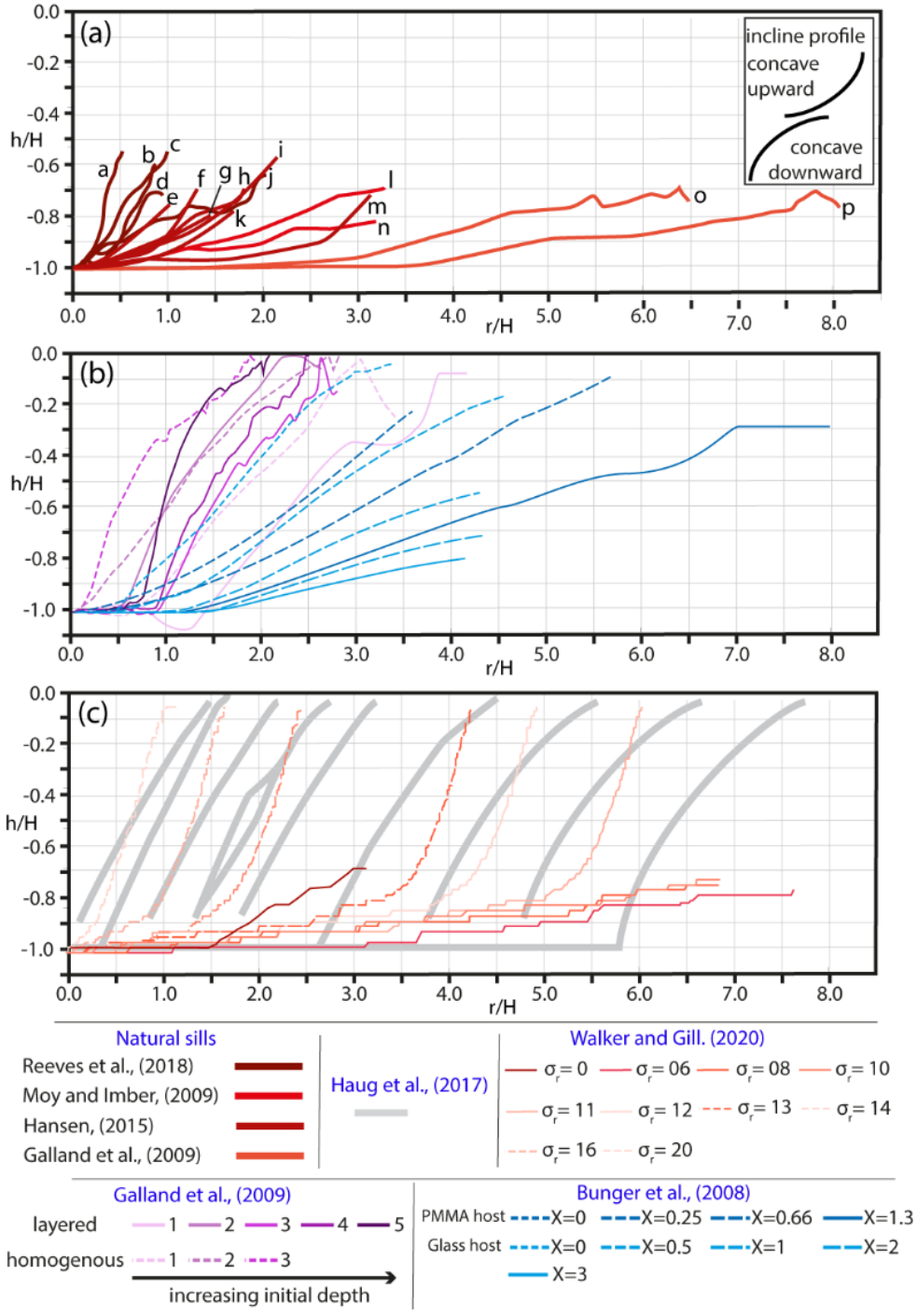

Figure 2. *A comparison of saucer-shaped sill geometry in (a) nature, (b) experimental and (c) numerical models (modified after Walker and Gill, 2020). The axes plot sill radius (r) against intrusion depth (h), normalised by the overburden depth (H). Experiments by Galland et al. (2009) (purple curves in Fig. 2b) used elasto-plastic silica powder as the host-rock analogue, while Bunger et al. (2008) used brittle-elastic glass or polymethyl methacrylate (PMMA) (blue curves in Fig. 9b). Numerical models by Walker and Gill (2020) (red curves in Fig. 2c) investigated how a horizontal compressive tectonic stress (σ_r) in an elastic host influences saucer-shaped sill geometries. Haug et al. (2017) used a rigid-plasticity approach to simulate sills in homogenous Mohr-Coulomb material – grey curves in Fig. 2c plot damage zones, where magma is expected to intrude the host rocks, formed by inflation of horizontal cracks of variable starting length. Labels of saucer-shaped sills in nature represent; (a) Sill 2, (b) Sill 1, (c) Sill 3 and (d) Sill 4 in Canterbury Basin, offshore SE New Zealand (Reeves et al., 2018); (e) Morskranes Sill, (f) Sundini Sill, (g) Kvívík Sill, (h) Fugloy Sill, (i) Eysturoy Sill, (k) Streymoy Sill and (m) Svínoy-Fugloy Sill in Faroe Islands (Hansen, 2015); (l) Eocene Sill 1 and (n) Eocene Sill 2 in Faroe-Shetland Basin (Moy and Imber, 2009); (o) Golden Valley Sill, South Africa and (p) Tulipan, Møre basin (Galland et al., 2009).*

All of these saucer-shaped sill emplacement models assume ideally elastic or plastic end member rheological behaviour of host rocks. However, Earth's crust is thought to behave as a complex visco-elastic-plastic material (Ranalli, 2001; Bertelsen et al., 2018). Therefore, the models summarised above are likely not able to fully simulate the natural diversity of intrusion geometries, including the formation of saucer-shaped sills. Moreover, some models require quite high horizontal stresses to get those in nature (Fig. 2) (Bunger et al., 2008; Gill and Walker, 2020; Walker and Gill, 2020).

Most saucer-shaped sills in nature form in sedimentary basins that contain mechanically layered strata (Rivalta et al., 2005; Kavanagh et al., 2018). Sill intrusions modelled by Kavanagh et al., (2006, 2015) show that a layered system with a stiffer upper layer is required to create experimental sills. According to their experimental results, a weaker interface and the

higher rigidity contrast (i.e., Young's modulus ratio) between the layers play major roles in the formation and propagation of sills. This has been further supported by analogue experiments of saucer-shaped intrusions using granular materials (Galland et al., 2009), which found that mechanical layering is required to create the inner sills of saucer-shaped intrusions. However, Galland et al. (2009) did not test the effects of rigidity contrasts on saucer-shaped intrusion formation and propagation. Therefore, the effect of layering and its mechanical properties such as the Young's modulus ratio on the emplacement of saucer-shaped intrusions remain poorly understood.

Although field and 3D seismic reflection data have yielded a wealth of information about the geometries of saucer-shaped sills, field observations are limited due to the lack of well-preserved outcrops. Furthermore, 3D reflection seismic observations are limited by their spatial resolution, making it challenging to characterize intrusion geometries and associated structures related to their propagation. The geometries and emplacement mechanisms of saucer-shaped sills are therefore still poorly constrained and many fundamental questions remain to be answered. Such as, is it possible to reproduce the geometry of natural saucer-shaped sills in the laboratory using host rock analogues with complex visco-elastic-plastic rheology? What emplacement mechanisms control the development of saucer-shaped sills within complex host rock analogues? How do rigidity contrasts between stratigraphic layers influence the propagation of intrusions? Are high horizontal stresses strictly required to form natural saucer-shaped geometries?

Answering these questions requires experiments that simulate injection of a viscous liquid into a visco-elastic-plastic host material, and the ability to analyse the geometry of the resulting intrusions and associated host rock deformation. In this paper, we document the results of laboratory experiments in which paraffin oil (the magma analogue) is injected into visco-elastic-plastic Laponite RD® gels, simulating the upper crust. Our objectives are to

simulate the emplacement of saucer-shaped sills and to better constrain the mechanisms governing their fundamental geometry, including the effects of mechanical layering. The complex segmentation patterns that are observed at the margins of our model sills are the subject of a companion paper (Arachchige et al., in review) and only briefly presented here.

2. Experimental methods

2.1. Experimental setup

Our experiments are designed to simulate the horizontal propagation of sills in the laboratory and to visualise the resulting lateral flow of analogue magma. The main objective of the experiments reported here is to investigate the emplacement and propagation of saucer-shaped intrusions in layered analogue host rocks. The experimental setup comprises a plexiglass tank (30 cm x 30 cm x 6 cm) filled with layers of Laponite RD® (LRD) gel as the upper crustal analogue (Layer 1 and Layer 2, Fig. 3). The upper surface of LRD in the tank is a free surface, while the vertical side walls and base of the tank are no-slip boundaries.

Paraffin oil (magma analogue) is injected horizontally into the LRD using a tapered needle (2 mm inner diameter) via a nozzle at the side of the tank fed by a peristaltic pump at a controlled volumetric flow rate. The experiments involve different volumetric flow rate of the intruding fluid, and the rigidity of the LRD layers. Fluid propagation is recorded by high resolution DSLR cameras (Fig. 3) placed above and at the side of the tank to capture the intrusion geometry and its evolution in plan and cross-sectional view, respectively.

2.2. Image processing

We use blue-channel pixel intensity values to map contour lines of the intrusion margin over time. Pixel intensity values at each time step (I) are normalised by pixel intensity values at time step 0 (before the intrusion starts) (I_0), resulting in $I/I_0 = 1$ for the LRD host and $I/I_0 < 1$ for the intruding fluid. The I/I_0 ratio is used to define a threshold for the intruding fluid, which is used to determine growth contour lines using a built-in ‘contour’ function in MATLAB.

Since growth contours have irregular shapes, we calculate best-fit circles to the contour line at each time step and use the resulting radius to quantify horizontal sill growth rates. However, the intrusion radius measurements are not corrected for the slope of the outer sill. Since the images are captured in map view, growth contours for inclined outer sheet intrusions therefore appear closer.

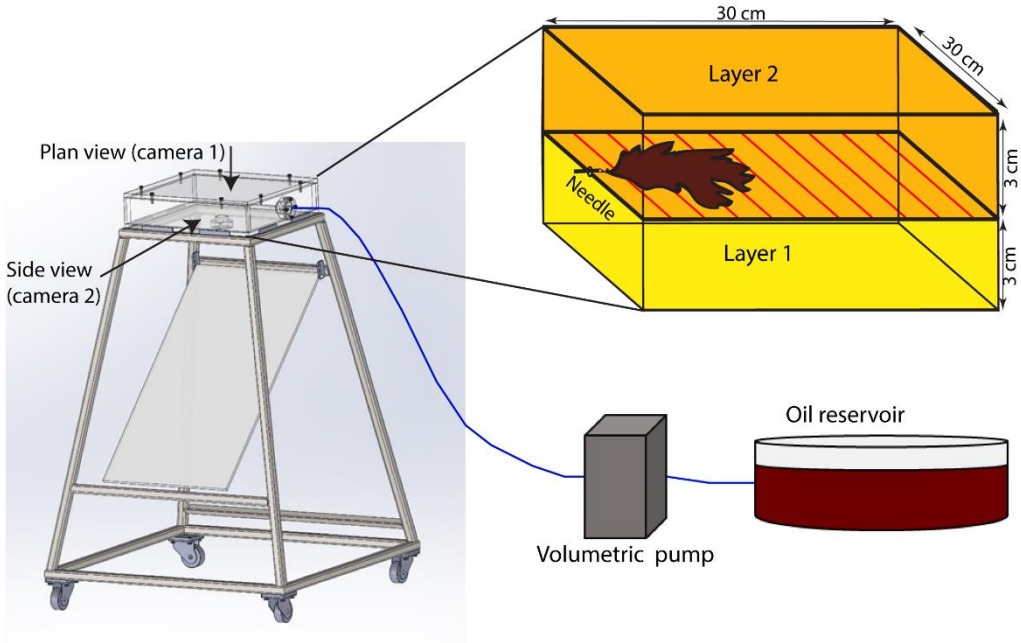

Figure 3. *Schematic diagram of the experimental setup used in this study. A volumetric peristaltic pump injects paraffin oil horizontally via a needle into either homogenous or two-layer Laponite RD® gel. Two DSLR cameras capture the geometric details of sill propagation from top and side views.*

2.3. Analogue materials

2.3.1. Crustal host rock analogue

The host rock analogue used in the experiments is Laponite RD® (LRD), a gel-forming grade of synthetic smectite clay manufactured by BYK Additives and Instruments (2014). Depending on its concentration, curing time and pH, LRD displays a wide range of viscoelastic properties, with purely elastic and viscous domains (Bonn et al., 2002; Ruzicka and Zaccarelli, 2011; Kaushal and Joshi, 2014; Arachchige et al., 2021). When mixed with water, LRD forms

a transparent gel, which is similar to gelatine but is colourless and more transparent. Like gelatine, its photo-elastic properties can be used to visualize and map stresses associated with propagating fractures. LRD is a chemically and biologically stable material and it is easy to alter its mechanical properties, such as the Young's modulus, by changing its concentration. LRD has lower surface energy values (24 - 44 mJ/m^2; Norris et al., 1993) compared to gelatine, a frequently used intrusion host rock analogue (1 J/m^2; Kavanagh et al., 2013). This ensures that surface tension dynamics are minimized in geological analogue experiments using LRD. Rheological measurements of LRD reported by Arachchige et al. (2021) indicate that it is suitable for modelling the visco-elastic-plastic deformation of rocks, including elastic and plastic end members. Linear visco-elastic (LVE) behaviour occurs for shear strains, $\gamma < 10\%$ and strain rates of up to 0.01 s^{-1} for concentrations from 2 wt. % to 4 wt. % and a curing time of 72 hours. LRD starts to yield at shear strain $\gamma = 10$ % for concentrations 2 wt. % to 4 wt. % with yield strength of 25 to 200 Pa, respectively. Higher shear strains ($\gamma > 26.2$ %) and strain rate $\dot{\gamma} \geq 0.01\ s^{-1}$ must be maintained to model plastic deformation. The Young's modulus of 2 wt. % to 4 wt. % LRD, with a curing time of 72 hours vary from 1.05×10^3 to 1.18×10^4 Pa, respectively. Here we use Young's modulus values of LRD as the main host rock variable and following Arachchige et al. (2021) assume that LRD is incompressible with Poisson's ratio = 0.5.

2.3.2. Magma analogue material

We use paraffin oil at 22.5 °C as the magma analogue due to its non-reactive stability with LRD. Paraffin oil has a viscosity of 0.16 Pa s and the density of 850 kg m^{-3} at this temperature. The magma analogue was mixed with red dye without altering its viscosity to provide a better visual contrast with the host material.

2.4. Scaling

Our experiments are approximately scaled to nature (Table 1) using methods developed by Hubbert (1937), Ramberg (1982), Merle and Borgia (1996), Mathieu et al. (2008), Galland et al. (2009) and Arachchige et al. (2021). The principle is to define scaling factors and dimensionless numbers for the model, which ensure approximate geometric, kinematic and dynamic similarity to processes in nature.

Table 1. *Symbols, units and values of variables in nature and model for scaling factors and dimensionless ratios. See equation 5 and 6 for Π_4 and Π_5.*

Parameter	Units	Definition	Value		
			Nature (p)	Model (m)	Ratio*(m/p)
ρ_c	kg m^{-3}	Density of host rock	2800	1000	0.357
ρ_m	kg m^{-3}	Density of magma	2700	850	0.3
G	m s^{-2}	Gravity acceleration	9.81	9.81	1
V_i	m s^{-1}	Velocity of intrusion	0.2	10^{-5}	$5 \cdot 10^{-5}$
L	m	Length	100	0.01	10^{-4}
t	s	Time	-	900-2700	$2 \cdot 10^{-2}$
μ	Pa s	Viscosity of intrusion	2.2 x 10^5	0.16	7.14 x 10^{-7}
Q_i	m^3 s^{-1}	Volumetric flow rate of intrusion	(0.02 - 13.28)	8.3 x 10^{-9}	(6.25 x 10^{-10} - 3.75 x 10^{-7})

	Definition of dimensionless ratios	Nature	Experiment
Π_1	Intrusion thickness (T)/length (L)	~ 10^{-2}	~ 10^{-2}
Π_2	Intrusion thickness (T)/depth (H)	0.06 – 0.66	0.03 – 0.10
Π_3	Intrusion height (h)/length (L)	0.2 – 0.3	0.3
Π_4	Inertial/viscous forces	2.5 x 10^{-6} – 270	(5.6 – 12.4) x 10^{-4}
Π_5	Magma/country rock densities	−0.08 – 0	0.14

Stress scaling factor	**$\sigma^* = \rho^* g^* L^* = 3.57 \times 10^{-5}$** Model is 10^5 times weaker than in nature
Time scaling factor	**$t^* = L^*/V^* = 2 \times 10^{-2}$** 1 min in model ~ 0.83 hr in nature
Viscosity scaling factor	**$\mu^* = t^* \sigma^* = 7.14 \times 10^{-7}$** Model intrusion represents a magma viscosity of 10^4 Pas
Volumetric flow rate scaling factor	**$Q^* = \Delta\rho^* L^{*3} E^{*-1} V^* = 6.25 \times 10^{-10} - 3.75 \times 10^{-7}$ $m^3 s^{-1}$** Model volumetric flow rates = 0.02 – 13.28 $m^3 s^{-1}$ in nature

We define the length scale factor (L*) as the ratio between the overburden depth of the sill in the model (subscript m) to one in the shallow crust (subscript p), which is initially taken

as 10^{-4} (1 cm represents 100 m). The ratio between the density of LRD in our experiments and that of the natural host rocks (ρ^*) is ~ 0.36 and the gravitational acceleration is the same in our experiments and in nature ($g^* = 1$). Thus, the stress scaling factor is:

$$\sigma^* = \rho^* g^* L^* = 3.6 \times 10^{-5} \quad (1)$$

Comparing the average model intrusion tip velocity of ~ 1×10^{-3} ms^{-1} to an estimated natural magmatic intrusion velocity of 0.2 ms^{-1} (range between 0.1 ms^{-1} and 0.5 ms^{-1}; Spence and Turcotte, 1985; Kavanagh et al., 2013) gives a velocity scaling factor, $V^* = 5 \times 10^{-3}$. We can now define the time scaling factor as

$$t^* = L^*/V^* = 2 \times 10^{-2} \quad (2)$$

Therefore, 1 min in our experiments represents 50 min in nature. Using σ^* and t^*, the viscosity scaling factor becomes

$$\eta^* = \sigma^* t^* = 7.2 \times 10^{-7} \quad (3)$$

So paraffin oil (magma analogue) with a viscosity of 0.16 Pas is equivalent to a magma in nature with a viscosity of 10^4 Pas, consistent with basaltic andesite with low crystal content (Persikov, 1991; Mathieu et al., 2008).

The measured Young's modulus, E, of LRD concentrations after 7 days curing time used in the experiments is 10^3 - 10^4 Pa (see Arachchige et al., 2021). Since E of upper crustal sedimentary rocks is typically in the range of 10^9 - 10^{10} Pa (Kavanagh et al., 2013), the Young's modulus scaling factor, E^* in our experiments is $10^{-7} – 10^{-5}$. Therefore, based on σ^* and E^* our model host rock is ~10^5 times weaker than in nature.

With the exception of one experiment (10A), the volumetric flow rate of intruding magma in our experiments is kept constant, and only the Young's modulus of the host rock layers is varied between experiments. The only input geometric variable is the Layer 2 overburden depth, H (Fig. 2). Output geometric variables are the intrusion length, L, thickness,

T, and the vertical height of the intrusion (i.e., intrusion depth), h, relative to the interface between the horizontal layers or the injection needle.

Following the Buckingham-Π theorem (Barenblatt, 2003; Galland et al., 2009), we define five independent dimensionless numbers that characterise the system (Table 1), which are used to assess the geometrical, kinematic and dynamic similarities between the experiments and nature. The first three dimensionless numbers are the geometric ratios of the system:

$$\Pi_1 = T/L,$$
$$\Pi_2 = T/H, \quad (4)$$
$$\Pi_3 = h/L.$$

The length, L, and the thickness, T, of shallow crustal sills in nature are typically in the range of 10 – 100's km and 20 – 200 m respectively (Galland et al., 2009; Cruden et al, 2017). Therefore, Π_1 in nature is in the order of 10^{-2}. Experimental sill lengths and thicknesses vary between 5 – 9 cm and 1 – 3 mm, respectively, so Π_1 is also on the order of 10^{-2}. Overburden depth, D, is 3 cm in the experiments and 100 – 3000 m in nature. Thus, Π_2 ranges between 0.03 – 0.1 and 0.006 – 2 in the experiments and nature, respectively. Calculated Π_3 values range from 0.22 to 0.56 for the experiments, and are estimated to be around 0.3 in nature (Mathieu et al., 2008). The geometric dimensionless numbers of the models are therefore close to the natural values, indicating approximate geometric similarity.

The Reynolds number, which is the ratio of inertial to viscous forces in a flow, establishes if the flow regime within the intrusion is laminar or turbulent:

$$\Pi_4 = Re = \frac{\rho_m T V}{\eta} \quad (5)$$

where ρ_m is the density and η is the viscosity of magma. In the experiments, Π_4 varies between 8×10^{-3} to 1.6×10^{-2}. Therefore, viscous forces are dominant, inertial forces are negligible and the flow is laminar (i.e., Re << 2300). Reynolds numbers for magma flow within dykes and

sills in nature varies from 2.5×10^{-6} to 270 for felsic and mafic magma respectively (Galland et al., 2009). Therefore, the Reynolds numbers in our experiments are consistent with those in nature, where magma flow is usually laminar.

The final dimensionless number is the ratio of the magma and the host rock density, corresponding to the buoyancy of the magma, which can be expressed by:

$$\Pi_5 = 1 - \frac{\rho_m}{\rho_c} \quad (6)$$

Where ρ_c the density of the upper crustal host rocks. In our experiments, $\Pi_5 = 0.15$ and in nature it varies between -0.8 to 0 in the shallow crust (Galland et al., 2009), indicating that magma is neutrally to negatively buoyant. In the experiments the analogue magma is slightly positively buoyant. However, as most sills form and propagate as horizontal to sub-horizontal cracks, buoyancy effects are negligible (Lister and Kerr, 1991; Kavanagh et al., 2006; Galland et al., 2009) in both nature and experiments.

3. Experimental results

Here we present the outcomes of experiments with two different initial setups. In the first setup, the upper crust is represented by a single homogeneous layer. In the second setup, the crust comprises two layers with different LRD concentrations and therefore different Young's moduli (Table 2). In both setups the viscosity of the intruding fluid and the intrusion depth were kept constant, as was the volumetric injection rate, with the exception of Exp. 10A.

3.1. Single layer experiments

When paraffin oil was injected into homogenous LRD with concentration of 3 wt. % (Exp. 7, Table 2), the intrusion formed a horizontal crack (i.e., a sill) that propagated away from the injection point and then at ~360 s deviated upwards toward the free surface as a steeply inclined sheet (Fig. 4a). The propagating front of the intrusion developed irregular finger-like protrusions at the onset of steep upward propagation. At this stage, a narrow high-flow channel

348 also started to form from the injection point, which migrated through the flat sill into the
349 inclined sheet (Fig. 4a).

350 ***Table 2.*** *Summary of experiments and parameters*

No	X_{LL}	ρ_{LL}	E_{LL}	X_{UL}	ρ_{UL}	E_{UL}	E_{UL}/E_{LL}	θ	comments
7	3	1050	5013	-	-	-	-	71	Planar crack
3	2.5	1045	2405	4	1075	10266	4.27	-	Vertical crack in bottom layer
5	3	1050	5013	4	1075	10266	2.05	18.5	Flat sill to inclined saucer
6	3	1050	5013	3	1050	5013	1	17.8	Flat sill to inclined saucer
9	3.5	1060	8317	4	1075	10266	1.23	21.7	Flat sill to inclined saucer
10	4	1075	10266	4	1075	10266	1	16.3	Flat sill to inclined saucer
19	3.5	1060	8317	4	1075	10266	1.23	24.5	Flat sill to inclined saucer
23	2	1040	1216	4	1075	10266	8.44	-	Vertical crack in bottom layer
30	3.5	1075	8317	3.5	1060	8317	1	17.1	Flat sill to inclined saucer
10A[§]	4	1075	10266	4	1075	10266	1	19.5	Flat sill to inclined saucer

351 X = concentration of Laponite RD® (LRD) in deionised water (wt. %); ρ is density of LRD (kg m^{-3}); E
352 = Young's modulus of LRD (Pa); θ = inclination. E_{UL}/E_{LL} = rigidity ratio
353
354 Subscripts LL = lower layer and UL = Upper Layer.

355 [§]The injection volumetric flow rate in all experiments, Q = 1 ml/min, except experiment 10A where Q
356 = 5 ml/min

357

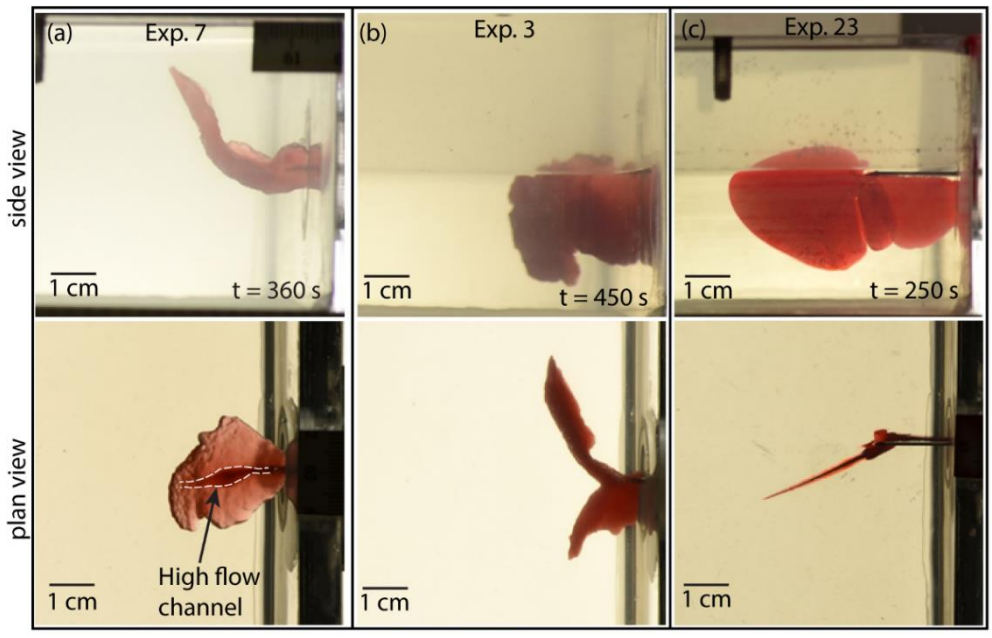

Figure 4. *(a) Intrusion propagation styles in a homogenous Laponite RD® gels with concentrations 3 wt. % (Exp. 7). (b) Plan and side views of layered experiments with high rigidity ratio (*$E_r > 4$*); Exp. 3 (left panel) and Exp. 23 (right panel). Vertical cracks (dykes) formed within the lower concentration (Layer 1). See Table 2 for experimental details.*

3.2. Two-layer experiments

In two-layer experiments, the magnitudes of the Young's moduli of the LRD layers (L1 and L2), and the rigidity ratio, $E_r = E_{UL}/E_{LL}$ were varied systematically, while the viscosity of the intruding fluid and the volumetric flow rate were kept constant, with the exception of Exp. 10A (Table 2). The non-dimensional Young's modulus ratio, E_r, was found to be useful for explaining the first-order morphology of the model intrusions. However, second order features of the intrusions, such as marginal lobes and fingers are controlled by additional parameters, which are discussed in more detail in Arachchige et al. (in review). In most two-layer experiments, an initially planar, sub-horizontal crack formed along the L1/L2 interface and, at a certain point, turned upwards to form an inclined sheet, making a saucer-shaped sill that eventually erupted at the upper free-surface. The behaviour for high and low rigidity ratios is markedly different and we will explore the details in the following two subsections.

3.2.1. Case 1: Two-layer experiments with high rigidity ratio ($E_r > 4$)

In two-layer experiments with a high rigidity ratio, $E_r > 4$ (Fig. 4b), the injected paraffin oil formed vertical cracks that propagated downwards from the injection point. These dyke-like intrusions were limited to the much weaker, lower layer, which had LRD concentrations $X_L = 2.5$ and 2 wt. % in Exp. 3 and 23, respectively (Fig. 4b; Table 2). The propagating fronts of these intrusions were smooth, without segmentation or finger-like protrusions.

3.2.2. Case 2: Two-layer experiments with low rigidity ratio ($E_r < 4$)

In all two-layer experiments with a lower rigidity ratio, $E_r < 4$, model intrusions initially propagated along the L1/L2 interface as inner flat, penny-shaped sills (Fig. 5a). These sills subsequently bent upwards together with overburden uplift as they intruded the upper layer,

forming inclined sheets (Fig. 5b and supplementary movie 1). The inclination, θ_i of these inclined sheets relative to the L1/L2 interface was 15° - 25°, becoming steeper as they approached the free surface (Fig. 5c). The propagating fronts of both the inner flat sill and the outer inclined sheets consisted of lobes and finger-like segments that appeared at early stages of growth. When primary individual lobes reach a critical width, they bifurcate into secondary smaller lobes and finger-like segments (Fig. 5d). During the propagation of the inner flat sill these lobes and fingers were confined to the 2D plane of the L1/L2 interface. However, once the inclined sheets entered the upper layer, these segments developed 3D morphologies, forming vertically offset, en-échelon structures (Fig. 5c)

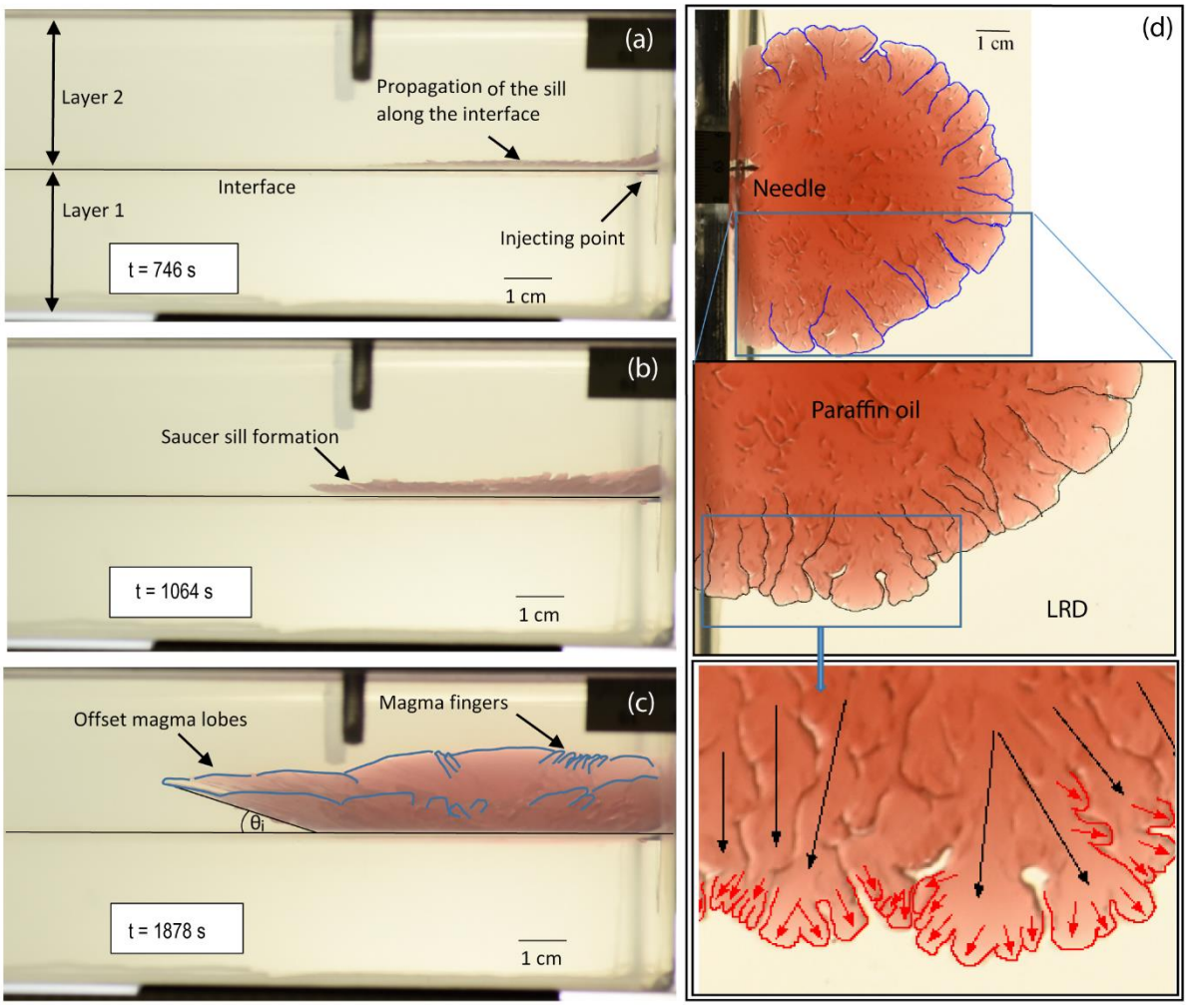

Figure 5. *Side views (left panels) and top views (right panels) of sill propagation in a two-layer experiment (Exp. 6) as a function of time (T). (a) Propagation of the inner sill along the two layer interface. (b) Onset of outer, inclined sill formation. (c) Offset lobes and fingers forming at the*

propagating sill margin. θ_i is the dip of the inclined sheet. (d) Formation and propagation of lobes and magma fingers and associated magma pathways. Paraffin oil (red) is injected from the left through a needle into transparent Laponite RD®. The sill expands radially and breaks into lobes and fingers. Lobe segments show distinct primary (blue) and secondary margins (black) and final magma transport directions (black and red arrows).

Figure 6 plots the vertical profiles of all saucer-shaped sills formed in the one- and two-layer experiments, in which the intrusion height (h) and the radius (r) are normalised by overburden depth (H). The transition radius from the inner sill to the outer inclined sheet occurs over a range of r/H values and the inclined sheets have variable inclinations, θ_i. The single layer experiment (Exp. 7) has the smallest transition radius (r/H < 0.5) and the steepest outer sheet inclination (71°). In two-layer experiments with $1 < E_r < 4$ (Exp. 5, 9 and 19), the transition radius occurs at r/H = 0.5 – 1.25, with much shallower outer sheet inclination angles (15°-25°). However, these inclination angles vary by 2° – 3° in Experiments 5, 9 and 19, indicating a small degree of uncertainty. Experiments 9 and 19 differ from experiment 5 in that E_{LL} is ~81% of E_{UL}, whereas in Experiment 5 this is ~ 49%. Therefore, sill inclinations are substantially different between experiments, reflecting the relative difference in stiffness between layers. In experiments with $E_r = 1$ (Exp. 6, 10, 10A, 30), the inner flat sills are considerably wider and the transition to the outer inclined sheet occurs at r/H = 1 - 1.5 with similar θ_i angles to the $1 < E_r < 4$ experiments. However, as the relative stiffness increases between Experiment 6 to 30, the inner sill appears to increase in length and the inclination angles are similar. By comparison, the only difference between Experiments 6 and 7 is the interface between the layers in Experiment 6, but it has a much longer inner flat sill with same inclination angle (Fig. 6).

3.3. Growth and propagation of the inner and outer sills

Growth contour maps of the propagating fronts of saucer-shaped sills with rigidity ratios $E_r < 4$ are shown in Figure 7. Because the maps are in plan view, growth contours within the inclined sheets appear more closely spaced than the inner flat section of the sill. Propagation

styles for experiments with $E_r = 1$ (Exp. 6, 30, 10) vary systematically as the absolute value of E and concentration of LRD increases within Layer 2. For $E_r = 1$ and an LRD concentration of 3 wt. % in L1 and L2 (Exp 6; Fig. 5d and 7a, Table 2), the intrusion propagated with a highly segmented margin characterised by finger-like and lobe structures. The absence of contours at early time steps is due to the unavailability of images due to a momentary camera failure. In Exp. 30 (Fig. 7b), with L_1 and L_2 concentration = 3.5 wt. %, growth contours indicate a propagation front with moderately developed segments. When the L_1 and L_2 LRD concentration = 4 wt. % in Exp. 10, the growth contours are smooth, indicating a planar propagation front with very weak to no segmentation (Fig. 7c). Two-layered experiments with $E_r > 1$ also have moderately segmented propagating fronts (Figs. 7d-f, similar to those in Exp. 30 (Fig.7b).

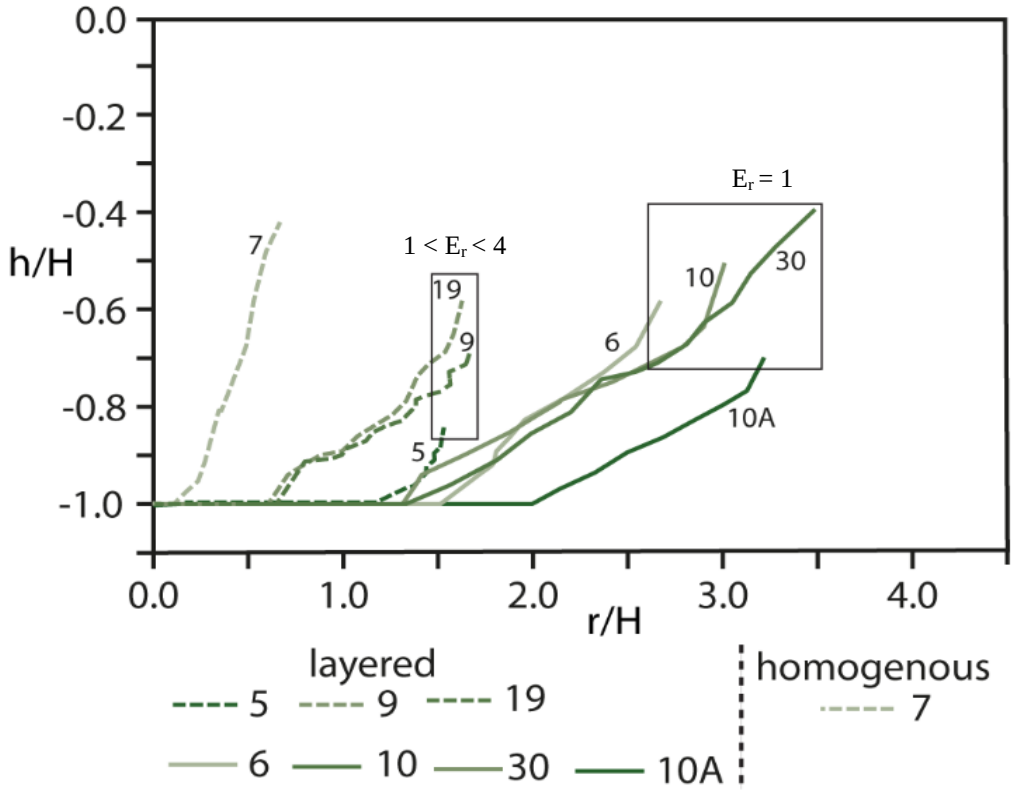

Figure 6. *Normalised vertical profiles of sills observed in homogeneous and two-layer experiments. The shortest inner sill and the steepest outer sill are formed by the homogenous layer experiment (Exp. 7). In layered experiments, the outer sill profiles are concave upward, becoming steeper toward the upper surface.*

The intrusion radius measured in plan view from best fit circles to the growth contours at each time step are plotted against time in Figure 8 for all two-layer experiments with $E_r < 4$. The inner-outer sill transition radius is marked for each experiment (i.e. black dotted line). The horizontal growth rates (i.e. slopes) of the intrusions with $Q_i = 1$ ml/min vary between 0.45 and 0.55 mm/s.

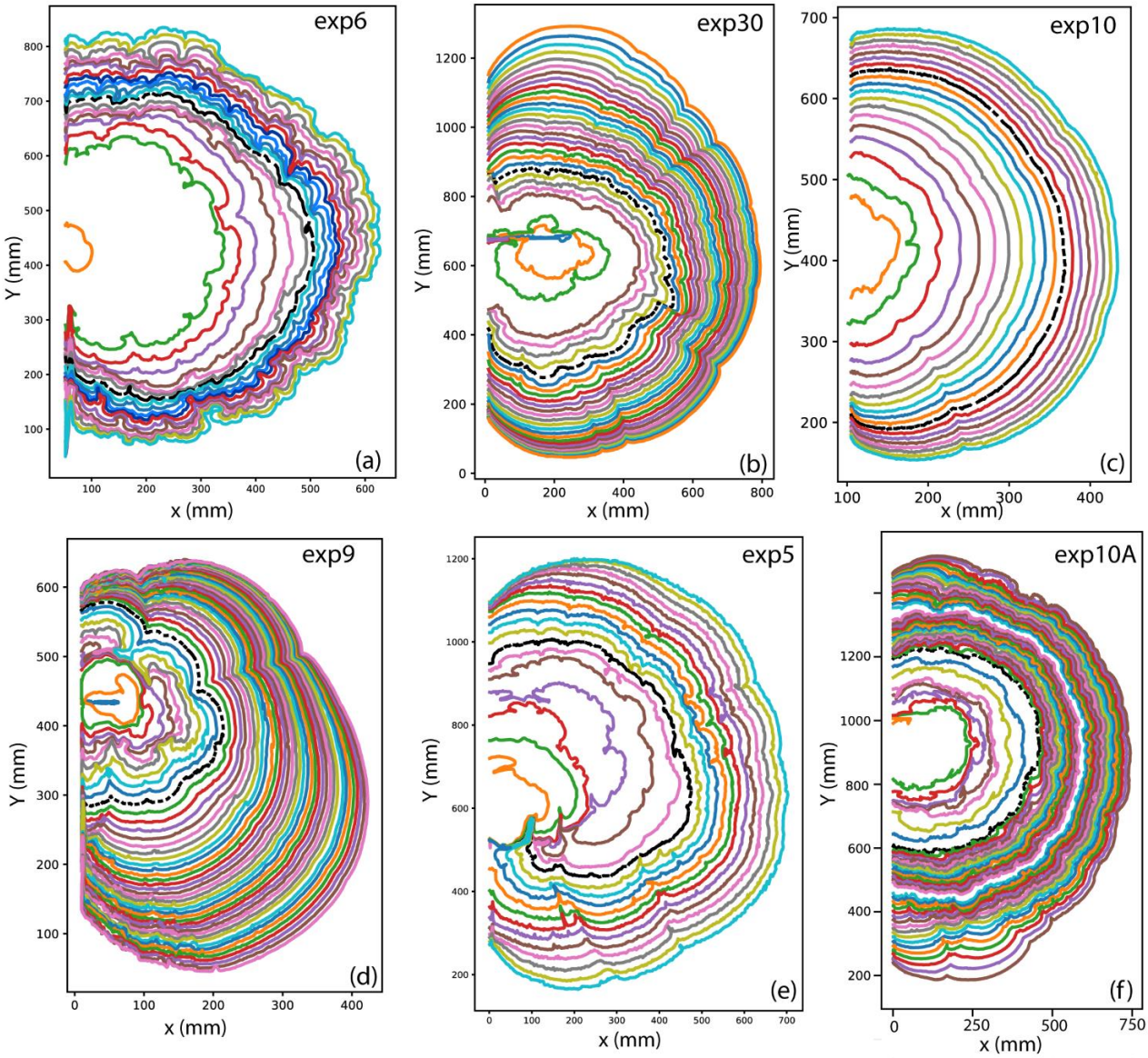

Figure 7. *Contour maps of sill margins over time calculated with image analysis. The contour interval is 25 s for all panels except exp.10A (10 s) and the dotted black contours on each map represent the contour at the inner to outer sill transition. The empty space in (a) (Exp. 6) is due to missing images due to camera failure at the early stages of the experiment.*

3.4. Influence of volumetric flow rate, Q_i

To determine the effect of a higher volumetric injection flow rate, we repeated Exp. 10 (Fig. 7c) in Exp. 10A with Q_i = 5 ml/min rather than 1 ml/min. This resulted in the largest inner-outer sill transition radius r/H ~ 2 observed in the two-layer experiments and a similar θ_i angle (Fig. 6). As expected, the horizontal growth rate of Exp. 10A is higher than the experiments with Q_i = 1 ml/min, with a value of 0.61 mm/s compared to ~0.5 mm/s.

In contrast to the planar sill margin developed in Exp. 10, growth contours for Exp. 10A (Fig. 7f) indicate a complex and strongly segmented propagation front, similar to Exp. 6 (Fig. 7a). This implies that the nature of the propagating front is controlled not only by the absolute value of E in Layers 1 and 2 (cf. Figs. 7a-c and f), but also on the volumetric injection flow rate of the analogue magma.

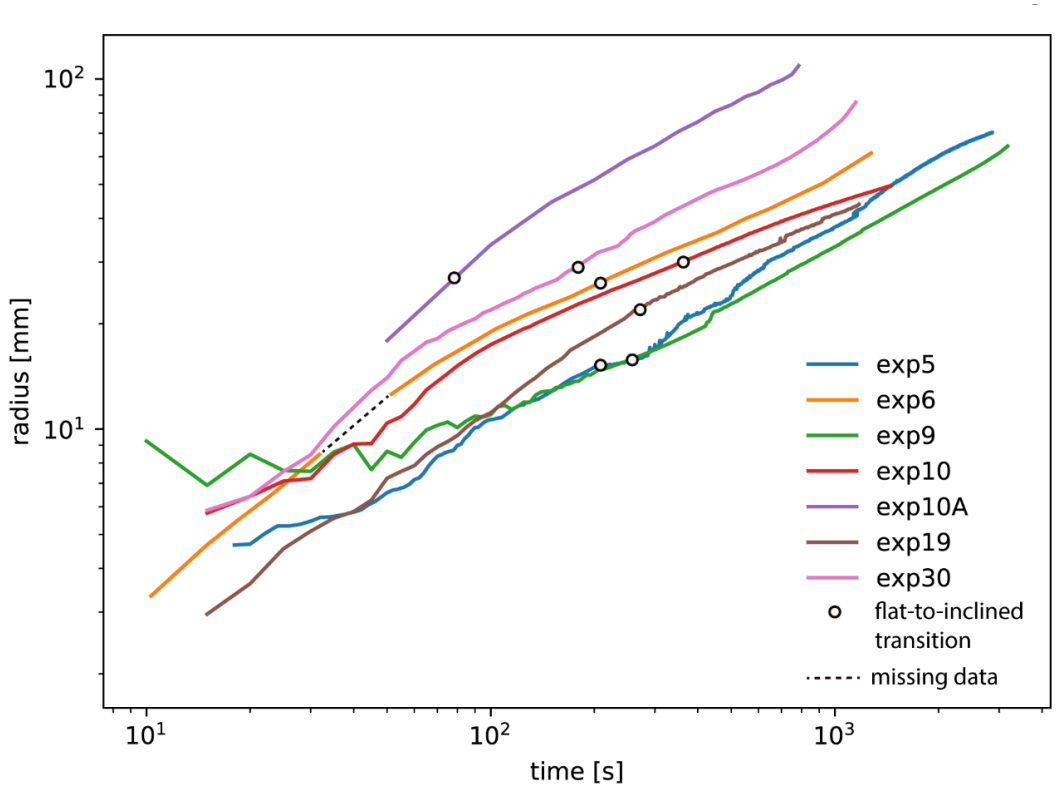

Figure 8. *The average radius for sills in experiments (in map view) with rigidity ratio* $E_r < 4$ *plotted as the best fit radius against time. The black open circles on each curve represent the transition from inner flat sill to inclined sheet of saucer-shaped intrusions. See Table 2 for the details of the experiments.*

4. Discussion

4.1. General considerations

The first-order geometries (i.e. saucer-shape, sill inclination) of intrusions formed in our experiments match the major features of mafic sills observed in nature, particularly those in sedimentary basins. Our homogenous and two-layer experiments (except the vertical dyke in Exp. 4b) reproduced the three-dimensional shape of saucer-shaped sills with a horizontal inner sill, emplaced along a horizontal interface in two-layer experiments, followed by a sharp transition to an outer, inclined sheet. Furthermore, the margins of both inner sills and outer inclined sheets in the experiments developed non-planar intrusion fronts with lobes and finger-like structures that are similar to marginal features of saucer-shaped sills observed in 3D seismic reflection seismic data (Thomson and Hutton, 2004; Hansen and Cartwright, 2006) and the marginal lobes developed on propagating sills during solidification experiments (Chanceaux and Menand, 2016). Our 3D experimental results also support the results of 2D numerical simulations of saucer-shaped intrusions (Malthe-Sørenssen et al., 2004; Walker and Gill, 2020). We therefore suggest that our model results provide insights into mechanical processes governing the emplacement of mafic sills in sedimentary basins.

4.2. Emplacement of the inner sill

In homogenous layer experiments, paraffin oil that was injected into low and moderate concentrations of LRD formed either a spherical blob (Arachchige et al., 2021) or a very short inner sill followed by a very steep outer sheet (Fig. 4a), respectively. In contrast, in two-layer experiments with low rigidity ratio ($E_r < 4$), paraffin oil injection always resulted in the formation of flat inner sills with large diameters (Fig. 4), whereas in experiments with high rigidity ratio ($E_r \geq 4$), a sub-vertical intrusion propagated in the weaker lower layer only (L1; Exp. 3 and 23, Fig. 4b). These results suggest that the formation of larger diameter, flat-lying sills requires the presence of layering in host rocks with low rigidity ratios ($E_r < 4$). This

516 conclusion is supported by previous experiments with a layered setup (Kavanagh et al., 2006,
517 2015; Galland et al., 2009) and numerical calculations (Barnett and Gudmundsson, 2014). In
518 detail, the propagating margin of the inner sill in both homogenous and layered experiments is
519 typically non-planar and often consists of finger-like and lobate segments (Fig. 5d). Such
520 complex segmentation was not observed in previous laboratory experimental models of sills
521 using gelatine or granular host media (Mathieu et al., 2008; Galland et al., 2009; Kavanagh et
522 al., 2015). However they are often described from mafic sills in sedimentary basins (Magee et
523 al., 2016; Spacapan et al., 2017) and 3D seismic reflection data (Hansen and Cartwright, 2006).
524 A detailed discussion of these irregular short-wavelength (in relation to the total intrusion
525 length scale) features and their formation is beyond the scope of the present paper and they are
526 analysed in detail in Arachchige et al. (in review).

527 **4.3. Inner sill to inclined sheet transition**

528 The transition from a flat inner sill to an inclined outer sheet, characteristic of all saucer-
529 shaped sills, has been discussed in previous analytical, numerical and laboratory modelling
530 studies (Pollard and Holzhausen, 1979; Polteau et al., 2008; Galland et al., 2009; Gill and
531 Walker, 2020). These previously published models of saucer-shaped sills display either smooth
532 (curved) or sharp inner to outer sill transitions when the magma or magma analogue intrudes
533 homogenous or layered host rocks, respectively. Our experiments produce similar smooth (Figs.
534 4a, 6) and sharp (Figs. 5, 6) transitions in homogenous and two-layer experiments, respectively.
535 This suggests that layering exerts a primary control on the formation of sharp transitions to
536 inclined sheets, but it is not a prerequisite to form saucer-shaped sills. Field observations of
537 sills in layered host rocks also confirm the presence of sharp inner to outer sill transitions (e.g.
538 Chevallier and Woodford, 1999; Polteau et al., 2008).

539 Several hypotheses have been proposed to explain the mechanics of the inner to outer
540 sill transition. Inspired by the behaviour of near surface hydraulic fractures, linear elastic

fracture mechanics (LEFM) approaches interpret this transition in the framework of the interaction between horizontally growing cracks and Earth's free surface (Pollard and Holzhausen, 1979; Fialko et al., 2001; Malthe-sørenssen et al., 2004; Bunger and Detournay, 2005; Bunger et al., 2005, 2008; Gill and Walker, 2020). Numerical experiments by Malthe-Sørenssen et al. (2004) show that when sills reach a radius approximately equal to the overburden depth (i.e., r/H ~ 1), their shapes start to become asymmetrical, which results in inflation induced bending of the overburden. Consequently, the stress in front of the sill tip becomes asymmetrical and the sill branches upwards. Fialko et al. (2001) theoretically predicted that the inclination, θ_i, of the outer sill should vary from 1° to 35° as r/H changes from 0.5 to 5, respectively. These theoretical θ_i values are within the range of those observed in natural saucer-shaped sills, where θ_i = 10° to 30° (Malthe-Sørenssen. et al., 2004; Galland et al., 2009).

In comparison, in assuming that the host rocks are Mohr-Coulomb materials, numerical analysis by Haug et al. (2017) suggests that the inner to outer sill transition occurs due to the formation of a localized plastic shear damage zone (or shear failure zone) at the tip of a growing sill. In this model, the inflating inner flat sill triggers the formation of shear failure zones that propagate from the sill tip to the Earth's surface, which then provides an inclined pathway for subsequent magma flow and outer sill formation. However, all of the saucer-shaped sill profiles of Haug et al. (2017) have inclination angles, $\theta_i \geq 60°$, which is much steeper than those observed in nature. The magma overpressure required for shear failure of the overburden in Haug et al.'s (2017) model varies from 100's of MPa to 60MPa for sills with r < 2 km and a few MPa for larger sills with r > 2 km. However, magma overpressure estimates in nature are typically in the range of 1 – 20 MPa (Rubin, 1995). Therefore, Haug et al. (2017) argue that localized shear failure of the overburden is only favoured for larger sills (r > 2 km) when r/H >1. Localized shear failure of the overburden during saucer-shaped sill formation has also been

reproduced in laboratory experiments that used Mohr-Coulomb, elasto-plastic host rock analogues, in which the formation of inclined outer sheets was attributed to plastic deformation and the formation of shear zones (Galland et al., 2009; Mathieu et al., 2008).

In comparison, our experimental saucer-shaped sills have outer sill inclination angles, $\theta_i = 15° – 25°$ and the inner to outer sill transition occurs when $0.5 \leq r/H \leq 2.5$, with no evidence for shear faulting in the LRD host material at the onset of inclined sheet formation. Therefore, the experiments reported here do not support a model of inelastic damage as a mechanical precursor for inclined sheet emplacement. Our experimental results are more compatible with LEFM models, in which saucer-shaped sills form as a consequence of asymmetrical stress fields generated by inflation of the inner flat sill and its elastic interaction with its surroundings and the free surface (Pollard and Holzhausen, 1979; Malthe-Sørenssen et al., 2004). This is supported by the sill profiles in Figure 5, which show that the outer inclined sills start to propagate upwards when r/H reaches values of 0.5 to 2.5. At this point, the sills climb upward with shallow inclinations (i.e. $15° \leq \theta_i \leq 25°$) due to a change of the stress field, which is linked to the onset of overburden uplift.

4.4. Comparison of experimental and natural saucer-shaped sill profiles

Vertical profiles of the experimental sills reported here are compared with natural saucer-shaped sill profiles in Figure 9a (modified after Walker and Gill, 2020) in which the intrusion height, h, and radius, r, are normalised by the overburden depth, H. The inner sill to inclined outer sheet transition in natural saucer-shaped sills occurs when r/H = 1 to 4 (Fig 9a; Malthe-Sørenssen. et al., 2004; Galland et al., 2008) and the corresponding outer sill inclination angles, θ_i = 10 - 30°, are similar to our experimental results. Inclined outer sheets in nature typically initiate with a lower inclination angle that increases towards the surface, so they have concave upward profiles (Gill and Walker, 2020). Except for the Golden Valley and Tulipan Sills, which have r/H > 3.5 (Fig. 2a), all of the normalised natural saucer-shaped sill profiles

plotted in Figure 9a share similar geometric features (i.e., h/H and r/H ratios, θ_i angles and concave upward shapes) with our experimental results.

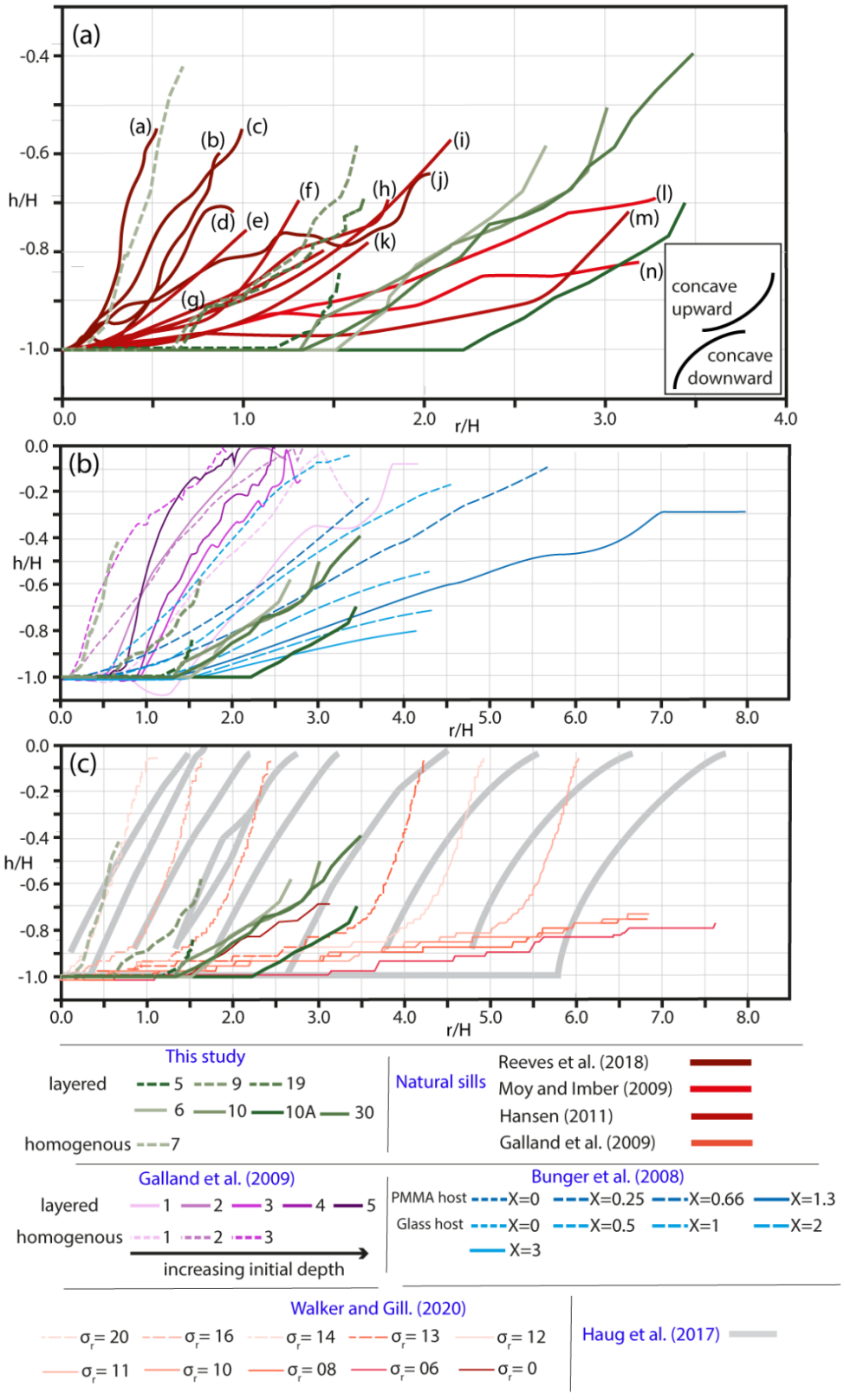

Figure 9. *A comparison of normalised saucer-shaped sill profiles from this study with (a) nature, (b) laboratory experimental and (c) numerical models (modified after Walker and Gill, 2020). Except for the Golden Valley and Tulipan Sills (Fig. 2a), saucer-shaped sill profiles in this study are similar to natural examples with concave upward shapes (Fig. 9a). See fig. 2 for the details of the saucer-shaped sills in nature (fig. 9a; a – o).*

The normalised profiles of saucer-shaped sills modelled in the laboratory by Bunger et al. (2008) and Galland et al. (2009) have steeper outer sill inclination angles with concave downward shapes in contrast to the experiments reported here (Fig. 9b). Bunger et al. (2008) used glass and polymethyl methacrylate (PMMA) as brittle-elastic host rock analogues and water, glycerine or glucose syrup as the magma analogue. They also introduced a dimensionless fracture toughness number, $\chi = \frac{\sigma_r \sqrt{H}}{K_c}$ where K_c is the fracture toughness of the host material (Fig. 8b). In their experiments, the inner to outer sill transition occurs when $0 \leq r/H \leq 2$, increasing with increasing χ-value (i.e., with increasing emplacement depth, horizontal compressive stress, or decreasing fracture toughness). Bunger et al.'s (2008) experimental sills have inclinations $15° < \theta_i < 30°$, which, except for their concave down profiles, is similar to both our model results and natural saucer-shaped sills (Fig. 9b).

Galland et al.'s (2009) laboratory experiments used elasto-plastic silica powder and vegetable oil as host rock and magma analogues, respectively (Fig. 9b). The injected oil formed cone sheets or vertical dykes within homogenous models whereas saucer-shaped intrusions formed in layered experiments. The inner to outer sill transition in their layered models occurs when $r/H \sim 0.5 - 1.5$ with outer sill inclinations $40° < \theta_i < 50°$. However, these inclinations are steeper than those in nature and they also have strongly concave downward profiles.

In the numerical experiments by Haug et al. (2017), the inner-outer sill transition is prescribed by a fixed initial sill radius, which varied effectively from ~ 0.5 to 6 km. In their models, the outer sheet inclinations (θ_i) adjacent to the inner sill are much steeper ($\theta_i \geq 60°$)

than that those observed in this study and in nature, and they also have strongly concave downward profiles (Fig. 9c).

Recent numerical modelling by Gill and Walker (2020) and Walker and Gill (2020) used axisymmetric finite-element calculations to investigate how a compressive horizontal tectonic stress (σ_r) changes the geometry and aspect ratio of saucer-shaped sills (Fig. 9c). Their model considered tensile fracture and shear failure crack tip separation mechanisms, and the input parameters were magma overpressure, host rock elasticity and the externally applied tectonic stress. In their analysis, when $\sigma_r = 0$ MPa, the inner to outer transition occurs when r/H = 1.5, $\theta_i \sim 25°$, and the resulting outer sheet has a concave upward profile, in good agreement with our results. Walker and Gill (2020) showed that as σ_r increases (0 MPa $\leq \sigma_r \leq$ 5 MPa), saucer-shaped sills form with increasingly wider inner sills (1.5 $\leq$ r/H $\leq$ 4.5) and shallower outer sill inclinations (25° < θ_i < 1°). However, for 5 MPa $\leq \sigma_r \leq$ 10 MPa, θ_i is constant at 1° and r/H reduces to 0.5 from 4.5 (Fig. 4 in Walker and Gill, 2020). Furthermore, they concluded that the model results for 5 MPa $\leq \sigma_r \leq$ 10 MPa show a good fit to natural saucer-shaped sills, and that the sill tips propagate by Mode I tensile failure. However, when $\sigma_r >$ 10 MPa, r/H < 0.5 and θ_i increases up to 45°, and sill tips propagate by host rock shear failure (Fig. 8c).

In many of the laboratory (Bunger et al., 2008; Galland et al., 2009) and numerical simulations (Haug et al., 2017) reviewed above, the resulting saucer-shaped sills have concave downward inclined outer sheets with steep inclination angles. This contrasts with inclined outer sheets in most natural examples, which are concave upward with shallow inclination angles (Walker and Gill, 2020) (Fig. 9a). Numerical simulations by Gill and Walker (2020) and Walker and Gill (2020) show that a strong compressive stress regime is required to match the geometry of natural saucer-shaped sills. However, the h/H and r/H ratios, outer sheet inclination angles and concave upward shapes observed in our experiments closely match the geometries of natural saucer-shaped sills, without the imposition of a horizontal tectonic stress.

Therefore, the experiments presented here highlight the importance of host-rock rheology (i.e., visco-elastic-plastic) for saucer-shaped sill formation, in addition to the possible contribution of horizontal stress boundary conditions.

5. Conclusions

We have described the results of laboratory modelling of saucer-shaped sill intrusions, in which paraffin oil (magma analogue) was injected at a constant volumetric flow rate into a homogenous or two-layer model crust made of visco-elastic-plastic Laponite RD® (LRD) gel. The resulting experimental saucer-shaped sills form by the interaction between the outwardly propagating and vertically inflating sill and the overburden its overlying free surface. Our main findings are:

1. Saucer-shaped sills emplaced into homogenous LRD have the shortest inner sill diameter, a smooth transition into inclined sheet and steeply inclined outer sill compared to two-layer experiments.

2. In two-layer experiments, saucer-shaped sills develop with a flat-lying inner sill that followed the L1/L2 interface and an inclined outer sheet that propagates through the upper layer towards the model surface. The inner sill to inclined outer sheet transition is sharp and occurs over a range of inner sill radius to overburden depth (r/H) ratios between 0.5 and 2, which increase with decreasing Young's modulus or rigidity ratio (E_r) and increasing volumetric injection rate.

3. The horizontal growth rate of all saucer-shaped sill intrusions is uniform for all values of E_r and a constant volumetric flux rate (Q_i = 1ml/min). However, for the same E_r, the growth rate increases when Q_i is increased (Exp 10A; Q_i = 5 ml/min).

4. The saucer-shaped sills that formed in our experiments are compatible with brittle-elastic (LEFM) models in which the inner sill to outer inclined sheet transition occurs due to an elasticity-dominated interaction between the growing inner sill and the surrounding material

and free surface. However, as discussed by Arachchige et al. (in review), marginal lobes and finger-like segments observed in most experiments are more likely linked to small-scale visco-plastic instabilities occurring at the tip of the propagating sills. This suggests the operation of scale-dependent deformation processes, with brittle-elastic (LEFM) processes dominating at the whole of intrusion scale and visco-plastic processes dominating at the crack tip scale.

5. Experiments suggest that there is no strict requirement of high horizontal stresses to form natural saucer-shaped sill geometries and show the importance of host rock rheology of making complex sill geometries.

Acknowledgements

We gratefully acknowledge support from an Australian Research Council Discovery Grant (DP190102422) to A.R.C. and a DIPRS PhD scholarship from Monash University (Melbourne) to U.S.N.A.

References

Arachchige, U.N., Cruden, A.R., Weinberg, R., 2021. Laponite gels - visco-elasto-plastic analogues for geological laboratory modelling. Tectonophysics 805, 228773. https://doi.org/10.1016/j.tecto.2021.228773

Barnett, Z.A., Gudmundsson, A., 2014. Numerical modelling of dykes de fl ected into sills to form a magma chamber. Journal of Volcanology and Geothermal Research 281, 1–11. https://doi.org/10.1016/j.jvolgeores.2014.05.018

Bertelsen, H.S., Rogers, B.D., Galland, O., Dumazer, G., Abbana Benanni, A., 2018. Laboratory Modeling of Coeval Brittle and Ductile Deformation During Magma Emplacement Into Viscoelastic Rocks. Frontiers in Earth Science 6. https://doi.org/10.3389/feart.2018.00199

Bonn, D., Tanase, S., Abou, B., Tanaka, H., Meunier, J., 2002. Laponite: Aging and shear rejuvenation of a colloidal glass. Physical Review Letters 89, 157011–157014.

https://doi.org/10.1103/PhysRevLett.89.015701

Bunger, A.P., Detournay, E., 2005. Asymptotic solution for a penny-shaped near-surface hydraulic fracture. Engineering Fracture Mechanics 72, 2468–2486. https://doi.org/10.1016/j.engfracmech.2005.03.005

Bunger, A.P., Detournay, E., Jeffrey, R.G., 2005. Étude Expérimentale Du Comportement En Bout D'Une Fracture Hydraulique Se Propageant Près D'Une Surface Libre. Comptes Rendus - Mecanique 333, 299–304. https://doi.org/10.1016/j.crme.2005.01.004

Bunger, A.P., Jeffrey, R.G., Detournay, E., 2008. Evolution and morphology of saucer-shaped sills in analogue experiments. Geological Society Special Publication 302, 109–120. https://doi.org/10.1144/SP302.8

Chanceaux, L., Menand, T., 2016. The effects of solidification on sill propagation dynamics and morphology. Earth and Planetary Science Letters 442, 39–50. https://doi.org/10.1016/j.epsl.2016.02.044

Chevallier, L., Woodford, A., 1999. Morpho-tectonics and mechanism of emplacement of the dolerite rings and sills of the western Karoo, South Africa. South African Journal of Geology 102, 43–54.

Cruden et al, 2017. Geometric Scaling of Tabular Igneous Intrusions: Implications for Emplacement and Growth. Advances in Volcanology 1–4. https://doi.org/10.1007/11157

Eide, C.H., Schofield, N., Jerram, D.A., Howell, J.A., 2017. Basin-scale architecture of deeply emplaced sill complexes: Jameson Land, East Greenland Christian. Journal of the Geological Society 174, 23–40. https://doi.org/10.1144/jgs2016-018

Fialko, Y., Khazan, Y., Simons, M., 2001. Deformation due to a pressurized horizontal circular crack in an elastic half-space, with applications to volcano geodesy. Geophysical Journal International 146, 181–190. https://doi.org/10.1046/j.1365-246X.2001.00452.x

Galland, O., Planke, S., Neumann, E.R., Malthe-Sørenssen, A., 2009. Experimental modelling

740 of shallow magma emplacement: Application to saucer-shaped intrusions. Earth and
741 Planetary Science Letters 277, 373–383. https://doi.org/10.1016/j.epsl.2008.11.003
742 Gill, S.P.A., Walker, R.J., 2020. The Roles of Elastic Properties, Magmatic Pressure, and
743 Tectonic Stress in Saucer-Shaped Sill Growth. Journal of Geophysical Research: Solid
744 Earth 125, 1–24. https://doi.org/10.1029/2019jb019041
745 Hansen, D.M., Cartwright, J., 2006. Saucer-shaped sill with lobate morphology revealed by 3D
746 seismic data: implications for resolving a shallow-level sill emplacement mechanism.
747 Journal of the Geological Society 163, 509–523. https://doi.org/10.1144/0016-764905-
748 073
749 Hansen, J., 2015. A numerical approach to sill emplacement in isotropic media: Do saucer-
750 shaped sills represent “natural” intrusive tendencies in the shallow crust? Tectonophysics
751 664, 125–138. https://doi.org/10.1016/j.tecto.2015.09.006
752 Haug, Ø.T., Galland, O., Souloumiac, P., Souche, A., Guldstrand, F., Schmiedel, T., 2017.
753 Inelastic damage as a mechanical precursor for the emplacement of saucer-shaped
754 intrusions. Geology 45, 1099–1102. https://doi.org/10.1130/G39361.1
755 Hutton, D.H.W., 2009. Insights into magmatism in volcanic margins: bridge structures and a
756 new mechanism of basic sill emplacement - Theron Mountains, Antarctica. Petroleum
757 Geoscience 15, 269–278. https://doi.org/10.1144/1354-079309-841
758 Kaushal, M., Joshi, Y.M., 2014. Linear viscoelasticity of soft glassy materials. Soft Matter 10,
759 1891–1894. https://doi.org/10.1039/c3sm52978a
760 Kavanagh, J.L., Boutelier, D., Cruden, A.R., 2015. The mechanics of sill inception,
761 propagation and growth: Experimental evidence for rapid reduction in magmatic
762 overpressure. Earth and Planetary Science Letters 421, 117–128.
763 https://doi.org/10.1016/j.epsl.2015.03.038
764 Kavanagh, J.L., Burns, A.J., Hilmi Hazim, S., Hignett, S., Wood, E.P., Martin, S.A., Dennis,

765 D.J.C.C., 2018. Challenging dyke ascent models using novel laboratory experiments:
766 Implications for reinterpreting evidence of magma ascent and volcanism. Journal of
767 Volcanology and Geothermal Research 354, 87–101.
768 https://doi.org/10.1016/j.jvolgeores.2018.01.002
769 Kavanagh, J.L., Menand, T., Daniels, K.A., 2013. Gelatine as a crustal analogue: Determining
770 elastic properties for modelling magmatic intrusions. Tectonophysics 582, 101–111.
771 https://doi.org/10.1016/j.tecto.2012.09.032
772 Kavanagh, J.L., Menand, T., Sparks, R.S.J., 2006. An experimental investigation of sill
773 formation and propagation in layered elastic media. Earth and Planetary Science Letters
774 245, 799–813. https://doi.org/10.1016/j.epsl.2006.03.025
775 Lister, J.R., Kerr, R.C., 1991. Fluid-mechanical models of crack propagation and their
776 application to magma transport in dykes. Journal of Geophysical Research 96, 10049.
777 https://doi.org/10.1029/91JB00600
778 Magee, C., Muirhead, J.D., Karvelas, A., Holford, S.P., Jackson, C.A.L., Bastow, I.D.,
779 Schofield, N., Stevenson, C.T.E., McLean, C., McCarthy, W., Shtukert, O., 2016. Lateral
780 magma flow in mafic sill complexes. Geosphere 12, 809–841.
781 https://doi.org/10.1130/GES01256.1
782 Malthe-Sørenssen, Planke, A., Svensen, S.H., Jamtveit, B., 2004. Formation of saucer-shaped
783 sills. Geological Society, London, Special Publications 234, 215–227.
784 Mathieu, L., van Wyk de Vries, B., Holohan, E.P., Troll, V.R., 2008. Dykes, cups, saucers and
785 sills: Analogue experiments on magma intrusion into brittle rocks. Earth and Planetary
786 Science Letters 271, 1–13. https://doi.org/10.1016/j.epsl.2008.02.020
787 Moy, D.J., Imber, J., 2009. A critical analysis of the structure and tectonic significance of rift-
788 oblique lineaments (’transfer zones’) in the Mesozoic-Cenozoic succession of the Faroe-
789 Shetland basin, NE Atlantic margin. Journal of the Geological Society 166, 831–844.

790 https://doi.org/10.1144/0016-76492009-010
791 Norris, J., Giese, R.F., Costanzo, P.M., Vanoss, C.J., 1993. The Surface Energies of Cation
792 Substituted Laponite. Clay Minerals 28, 1–11.
793 https://doi.org/10.1180/claymin.1993.028.1.01
794 Persikov, E.S., 1991. The Viscosity of Magmatic Liquids: Experiment, Generalized Patterns.
795 A Model for Calculation and Prediction. Applications. 1–40. https://doi.org/10.1007/978-
796 1-4612-3128-8_1
797 Pollard, D.D., Holzhausen, G., 1979. On the mechanical interaction between a fluid-filled
798 fracture and the earth's surface. Tectonophysics 53, 27–57. https://doi.org/10.1016/0040-
799 1951(79)90353-6
800 Pollard, D.D., Johnson, A.M., 1973. Mechanics of growth of some laccolithic intrusions in the
801 Henry mountains, Utah, II. Bending and failure of overburden layers and sill formation.
802 Tectonophysics 18, 311–354. https://doi.org/10.1016/0040-1951(73)90051-6
803 Pollard, D.D., Muller, O.H., Dockstader, D.R., 1975. The form and growth of fingered sheet
804 intrusions. Bulletin of the Geological Society of America 86, 351–363.
805 https://doi.org/10.1130/0016-7606(1975)86<351:TFAGOF>2.0.CO;2
806 Polteau, S., Mazzini, A., Galland, O., Planke, S., Malthe-Sørenssen, A., 2008. Saucer-shaped
807 intrusions: Occurrences, emplacement and implications. Earth and Planetary Science
808 Letters 266, 195–204. https://doi.org/10.1016/j.epsl.2007.11.015
809 Ranalli, G., 2001. Experimental tectonics: From Sir James Hall to the present. Journal of
810 Geodynamics 32, 65–76. https://doi.org/10.1016/S0264-3707(01)00023-0
811 Reeves, J., Magee, C., Jackson, C.A.L., 2018. Unravelling intrusion-induced forced fold kine-
812 matics and ground deformation using 3D seismic reflection data.
813 https://doi.org/https://doi .org/10.30909/vol.01.01.0117
814 Rivalta, E., B, M., Dahm, T., 2005. Buoyancy-driven fracture ascent : Experiments in layered

gelatine. 144, 273–285. https://doi.org/10.1016/j.jvolgeores.2004.11.030

Rubin, A.M., 1995. Propagation of magma-filled cracks. Annu. Rev. Earth Planet. Sci 287–336.

Ruzicka, B., Zaccarelli, E., 2011. A fresh look at the Laponite phase diagram. Soft Matter 7, 1268–1286. https://doi.org/10.1039/c0sm00590h

Spacapan, J.B., Galland, O., Leanza, H.A., Planke, S., 2017. Igneous sill and finger emplacement mechanism in shale-dominated formation: a field study at Cuesta del Chihuido, Neuquén Basin, Argentina. Journal of the Geological Society 174, 422–433. https://doi.org/10.1144/jgs2016-056

Spence, D.A., Turcotte, D.L., 1985. Magma-driven propagation of cracks. Journal of Geophysical Research 90, 575–580.

Thomson, K., Hutton, D., 2004. Geometry and growth of sill complexes: Insights using 3D seismic from the North Rockall Trough. Bulletin of Volcanology 66, 364–375. https://doi.org/10.1007/s00445-003-0320-z

Walker, R.J., Gill, S.P.A., 2020. Tectonic stress controls saucer-shaped sill geometry and emplacement mechanism. Geology 48, 898–902. https://doi.org/10.1130/G47604.1